

**Supporting Information**  
**Ultrafast Electron Cooling and Decay in Monolayer WS<sub>2</sub>**  
**Revealed by Time- and Energy-Resolved Photoemission**  
**Electron Microscopy**

*Yaolong Li,<sup>†,‡</sup> Wei Liu,<sup>†,‡</sup> Yunkun Wang,<sup>†,‡</sup> Zhaohang Xue,<sup>†,‡</sup> Yu-Chen Leng,<sup>#</sup> Aiqin Hu,<sup>†,‡</sup> Hong Yang,<sup>†,‡,§,¶</sup> Ping-Heng Tan,<sup>#</sup> Yunquan Liu,<sup>†,‡,§,¶</sup> Hiroaki Misawa,<sup>⊥,∇</sup> Quan Sun,<sup>⊥,\*</sup> Yunan Gao,<sup>†,‡,§,\*</sup> Xiaoyong Hu,<sup>†,‡,§,¶,\*</sup> and Qihuang Gong<sup>†,‡,§,¶</sup>*

<sup>†</sup>State Key Laboratory for Artificial Microstructure and Mesoscopic Physics, School of Physics, Peking University, Beijing 100871, China

<sup>‡</sup>Frontiers Science Center for Nano-optoelectronics & Collaborative Innovation Center of Quantum Matter, Beijing 100871, China

<sup>§</sup>Collaborative Innovation Center of Extreme Optics, Shanxi University, Taiyuan, Shanxi 030006, China

<sup>¶</sup>Beijing Academy of Quantum Information Sciences, Beijing 100193, China

<sup>#</sup>State Key Laboratory of Superlattices and Microstructures, Institute of Semiconductors, Chinese Academy of Sciences, Beijing 100083, China

<sup>⊥</sup>Research Institute for Electronic Science, Hokkaido University, Sapporo 001–0021, Japan

<sup>∇</sup>Center for Emergent Functional Matter Science, National Chiao Tung University, Hsinchu 30010, Taiwan

## Table of Contents:

1. AFM image of the supported WS<sub>2</sub>
2. PL and Raman characterizations
3. FDTD simulations on optical interference effect
4. Time resolution of the TR-PEEM measurements
5. PEEM measurements for the supported WS<sub>2</sub>
6. PEEM measurements for the suspended WS<sub>2</sub>
7. Movie of TR-PEEM signals for the supported WS<sub>2</sub>

### 1. AFM image of the supported WS<sub>2</sub>

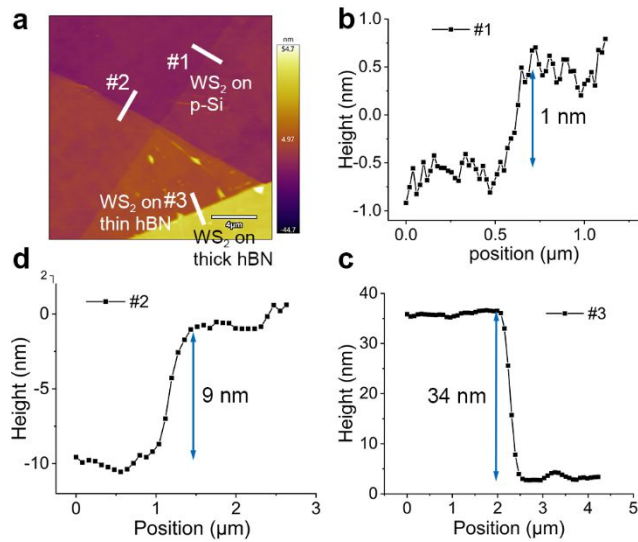


**Figure S1.** (a) AFM image of the supported monolayer WS<sub>2</sub> on p-Si and hBN (by Cypher VRS, Oxford Instruments). (b-c) Crosscuts from (a). The WS<sub>2</sub> was verified to be monolayer. The thicknesses of thin and thick hBN flakes are about 9 nm and 43 nm (9 nm + 34 nm), respectively.

### 2. PL and Raman characterizations

We measured the photoluminescence (PL) and Raman spectra to characterize the optical properties and sample quality.

The PL spectra were measured at room temperature using a continuous 532 nm laser, and an

inverted microscope (Eclipse Ti-2 inverted microscope, Nikon) equipped with an objective lens (40 $\times$ , NA = 0.6) and a spectrometer (Kymera 328i, Andor). The PL intensities are totally quenched on all the three regions for the supported WS<sub>2</sub> after PEEM measurements (Figure S2a). In contrast, the PL intensity is significantly strong even with much weaker excitation laser for the pristine WS<sub>2</sub> on PDMS (Figure S2b). The PL mapping of the suspended WS<sub>2</sub> after PEEM measurements and the extracted PL spectra along a yellow dashed line are shown in Figure S2c,d, in which the intensity variations across the hole are determined by both the optical interference effect induced by the underlying hole, and local defect density introduced during PEEM measurements. The PL intensity is also strongly quenched for the suspended WS<sub>2</sub> but still measurable, and the two peaks of PL spectra are attributed to A exciton (615 nm, 2.02 eV) and defect-bound exciton ( $\sim$  660 nm, 1.88 eV) (Figure S2e). Therefore, the PL spectra indicate the presence of defects on the supported and suspended WS<sub>2</sub> after PEEM measurements.

In order to avoid possible contamination during PL measurements, we didn't measure the PL spectra for the sample with WS<sub>2</sub> on hBN/Si investigated in the main text prior to PEEM measurements. Instead, we have measured PL spectra for other samples with monolayer WS<sub>2</sub> on Si and hBN following the same fabrication process. Figure S3 shows the PL spectra for samples of monolayer WS<sub>2</sub> on hBN/Si and on PDMS. As shown in Figure S3a and the inset of Figure S3c, the PL intensity for WS<sub>2</sub> on hBN/Si is weaker than on PDMS, probably due to the optical interference effect, as discussed by several publications.<sup>1, 2</sup> The peak shifts for WS<sub>2</sub> on different substrates, as shown in Figure S3c, are due to the difference in dielectric environment.<sup>3</sup>

The Raman spectra were measured at room temperature using a Jobin-Yvon HR800 micro-Raman system, equipped with a liquid-nitrogen-cooled charge couple detector (CCD) and an objective lens (100 $\times$ , NA = 0.90). The laser excitation wavelength was 488 nm from an Ar<sup>+</sup> laser. The 1800 lines/mm grating was used in the Raman measurements, which enabled each CCD pixel to cover 0.62cm<sup>-1</sup> at 488nm. A low laser power of 80  $\mu$ W was used to avoid heating and damaging. The Raman spectra for the supported and suspended WS<sub>2</sub> after PEEM measurements and another pristine WS<sub>2</sub> on PDMS are shown in Figure 3c and Figure S4. It

should be noted that, for the supported WS<sub>2</sub>, we measured the Raman spectra for WS<sub>2</sub> on the 43-nm hBN only, considering that the Raman signal could be very weak for WS<sub>2</sub> directly on p-Si because of the lack of Raman enhancement effect by optical interference.<sup>2, 4</sup>

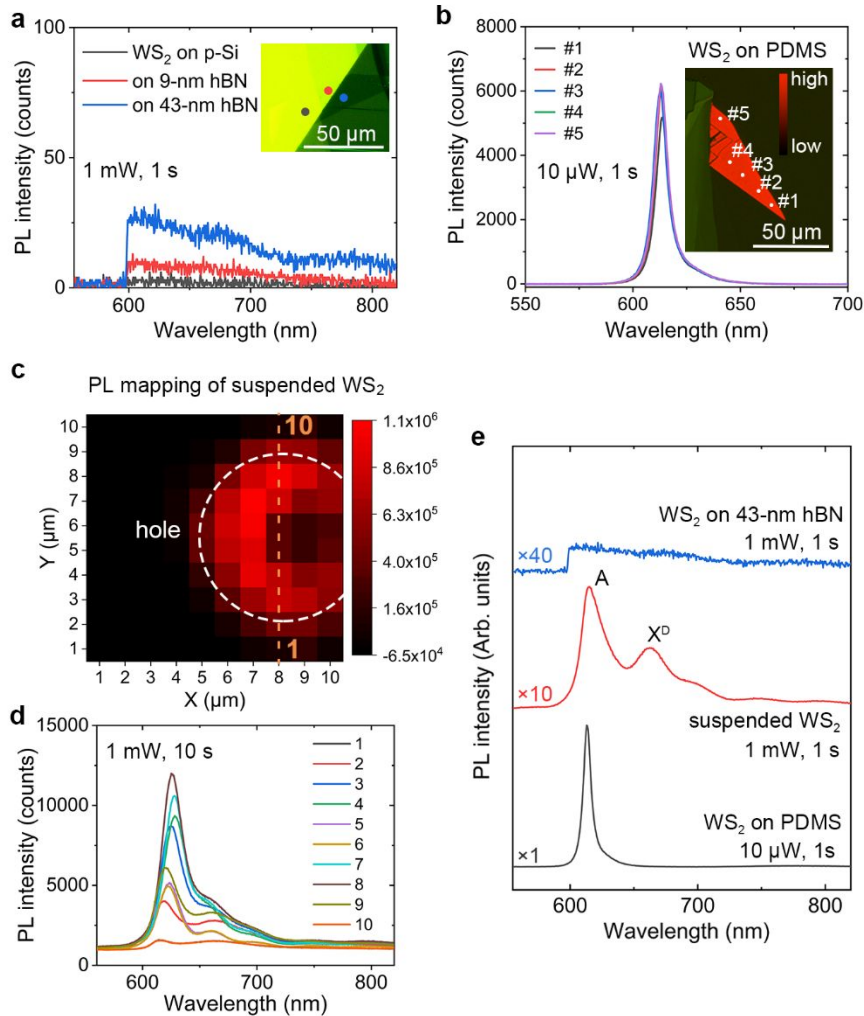


**Figure S2.** PL spectra for the supported and suspended WS<sub>2</sub> after PEEM measurements and the pristine WS<sub>2</sub> on PDMS. The power of excitation laser, and integration time are labeled. (a) PL spectra for the supported WS<sub>2</sub>. (b) PL spectra for the pristine WS<sub>2</sub>. (c) PL mapping of the suspended WS<sub>2</sub>, and the spectra along the crosscut are shown in (d). (e) Comparison of PL spectra.

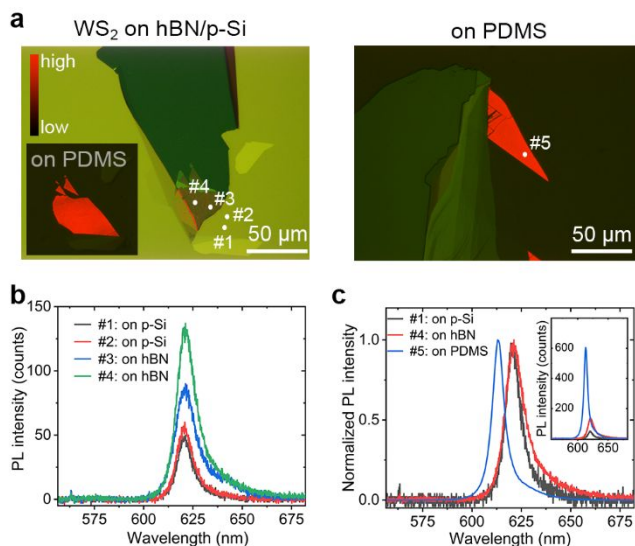


**Figure S3.** (a) Optical microscopy images (showing PL signals) for samples of monolayer WS<sub>2</sub> on hBN/Si and on PDMS without PEEM measurements. The inset in the left corner shows the image for the WS<sub>2</sub> before transferred to hBN/p-Si. (b) PL spectra for WS<sub>2</sub> on hBN/p-Si. (c) Comparison of the PL spectra. The PL spectra were measured with 532 nm CW laser with power of 1 μW and acquisition time of 1 s.

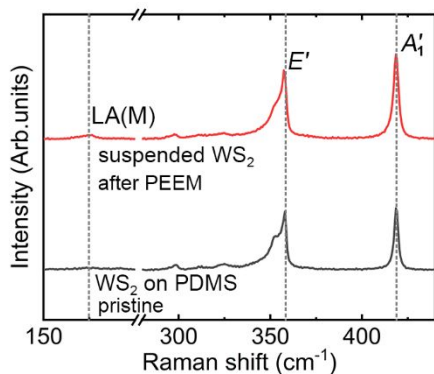


**Figure S4.** Raman spectra for the suspended WS<sub>2</sub> after PEEM measurements and the pristine WS<sub>2</sub> on PDMS.

The passivation of S-vacancy by oxygen adsorption has been reported by Nan et al.<sup>5</sup> Such a passivation mechanism can be enhanced by laser illumination in ambient condition, as reported in Ref.,<sup>6, 7</sup> the monolayer WS<sub>2</sub> or MoS<sub>2</sub> were found to exhibit considerable enhancement in the PL intensity after the laser treatments. They demonstrated that the enhancement arises from the healing of defects in monolayers via adsorption or substitution of the sulfur vacancies with oxygen. In our study, we observed a slight enhancement of PL intensity with laser treatment in

ambient condition for the monolayer WS<sub>2</sub> after PEEM measurements. Therefore, we speculate the PEEM measurement induced defects are of S-vacancies. As shown in Figure S5, the PL intensities were enhanced for the suspended WS<sub>2</sub> and another WS<sub>2</sub> samples after PEEM measurements during the PL measurements. Classification of defect types and the formation mechanism might need much more efforts to investigate in the future.

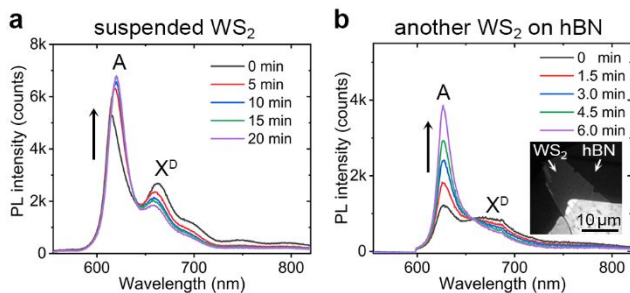


**Figure S5.** Enhancement of PL intensity with laser illumination time in ambient condition for monolayer WS<sub>2</sub> after PEEM measurements. (a) The suspended WS<sub>2</sub> investigated in the main text. (b) Another WS<sub>2</sub> sample on hBN after PEEM measurements (not shown in the main text), the PEEM image with excitation wavelengths of 410 nm (15 μJ/cm<sup>2</sup>) is shown as inset. The laser setup was the same as other PL measurements, and the laser was 532 nm CW laser with power of about 1 mW for (a) and 0.5 mW for (b) with spot diameter of 1~2 mm.

We have samples prepared with the same method and kept in the preparation chamber of PEEM (approximately 10<sup>-9</sup> Torr) for ~24 h without laser illumination, and found that the PL intensity was strong and no defect-related peak could be observed. Figure S6 shows the PL spectrum for WS<sub>2</sub> on hBN/20 nm SiO<sub>2</sub>/Si after this treatment. The PL intensity is comparable to that in Figure S3b, and the lower shoulder at ~638 nm is from trions. This measurement excluded the possibility of slow dark degradation of the sample in ultra-high vacuum. The degradation could be a combined effect, and the mechanism is not clarified yet.

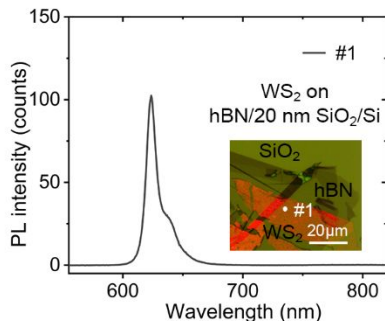


**Figure S6.** PL spectrum for WS<sub>2</sub> on hBN/20 nm SiO<sub>2</sub>/Si substrate (1 μW, 1 s). The two peaks are attributed to excitons and trions, respectively. The sample was kept in the preparation chamber of PEEM (approximately 10<sup>-9</sup> Torr) for ~24 h without laser illumination.

### 3. FDTD simulations on optical interference effect

To understand the experimental large contrast of PE intensity for the supported WS<sub>2</sub> on the three different regions of p-Si, 9-nm and 43-nm hBN, we simulated the near-field intensity on monolayer WS<sub>2</sub> with finite-difference time-domain (FDTD) solutions (Lumerical FDTD solutions) using the structure shown in Figure S7a, which is a typical film-interference structure. The refractive index of WS<sub>2</sub> was adopted from literature<sup>8</sup> and the thickness was set as 0.8 nm. The refractive index of hBN was set as 2.1.<sup>4</sup> The thickness of native SiO<sub>2</sub> layer on p-Si was set as 2 nm. The simulated electric field intensity  $|E|^2$  as a function of hBN thickness and wavelength is shown in Figure S7b. The extracted  $|E|^2$  for wavelengths of 273 nm and 410 nm are shown in Figure S7c, in which the intensities vary periodically with hBN thickness. By comparing the simulations with experiments, the large contrast of PE intensity is strongly correlated to optical interference effect. The quantitative difference between simulations and experiments was probably due to the parameter used in simulations, e.g. refractive index of hBN, and PE nonlinear order of WS<sub>2</sub>. The underlying substrate could also possibly modify the PE efficiency of WS<sub>2</sub>. In addition, the optical interference effect can also be clearly observed on the suspended WS<sub>2</sub>, as shown in Figure S14.

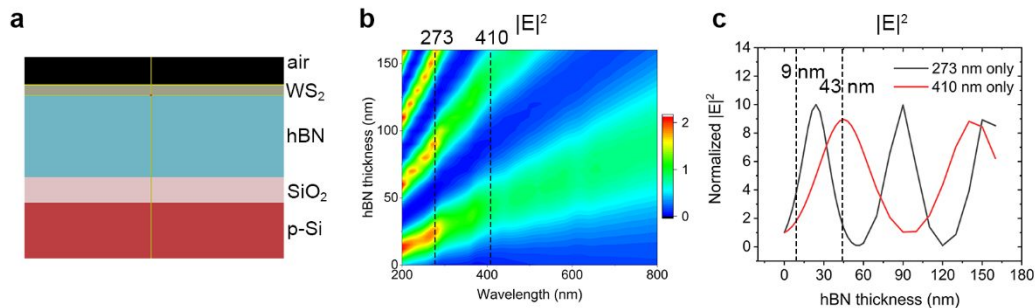


**Figure S7.** (a) Designed structure for FDTD simulations. (b) Mapping of electric field intensity  $|E|^2$  versus wavelength and hBN thickness. (c) Simulated electric field intensity of  $|E|^2$  on WS<sub>2</sub> layer as a function of hBN thickness for wavelengths of 273 nm and 410 nm, normalized by the intensity without hBN layer.

#### 4. Time resolution of the TR-PEEM measurements

The time resolution of the TR-PEEM system was evaluated by using the cross-correlation signals observed on the p-Si substrate during the pump–probe measurements. As shown in Figure S8a, a sharp peak was observed at the pump wavelength of 590 nm directly on the p-Si substrate. The sharp peak on the p-Si substrate was attributed to the cross-correlation signals between the pump and probe pulses because the following PE intensity was still increasing, which could be attributed to the slowly increased pump–probe signals on the p-Si. Similar to the intensity autocorrelation measurement, the cross-correlation measurement can be used to obtain the time resolution of the pump–probe system. Assuming Gaussian-shaped pump and probe pulses with intensities of  $I_1(t)$  and  $I_2(t)$ , the PE intensity induced by the cross correlation can be expressed as

$$PE(t) \propto \int_{-\infty}^{\infty} I_1(t)I_2(t-\tau)d\tau$$

$$= \frac{1}{\sqrt{2\pi(\sigma_1^2 + \sigma_2^2)}} \exp\left[-\frac{(t-\Delta t)^2}{2(\sigma_1^2 + \sigma_2^2)}\right], \quad (S1)$$

where  $\Delta t$  is the time delay between the pump and probe pulses and  $\sigma_1$  and  $\sigma_2$  are related to the durations of the two pulses. The fitted Gaussian-shaped PE intensity is shown in Figure S8b, which can be used to obtain the full width at half maximum (FWHM). Similar to the relation between the intensity autocorrelation width and pulse duration, the time resolution of our system was  $1/\sqrt{2}$  of the FWHM of the cross-correlation signal (approximately 200 fs). The time resolutions with other pump wavelengths were similar to this value.

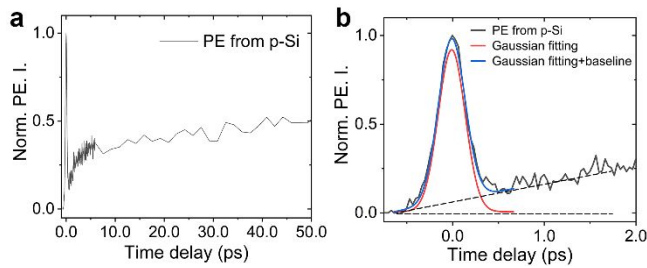


**Figure S8.** (a) Normalized TR-PEEM signal directly on the p-Si substrate (without WS<sub>2</sub>) with the excitation wavelength of 590 nm. (b) Enlarged view of the peak in (a), Gaussian fitting of the

peak (red line), and that with added baseline (blue line) to compare with the experimental data.

## 5. PEEM measurements for the supported WS<sub>2</sub>

The PE signals are dominantly from monolayer WS<sub>2</sub>. As shown in Figure S9, the PE intensity from p-Si (no WS<sub>2</sub>) is much weaker than that from WS<sub>2</sub> on p-Si and on hBN. Furthermore, the PE intensity is very sensitive to surface, the PE intensity from p-Si underneath WS<sub>2</sub> layer will be much weaker than that without WS<sub>2</sub>. Therefore, the signal from the underlying p-Si are negligible. In addition, the normalized PE intensity traces are independent of the pump fluence, as shown in Figure S10.

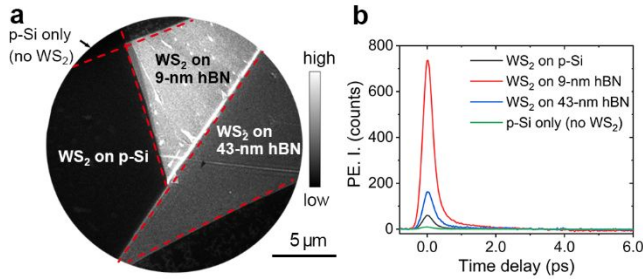


**Figure S9.** (a) PEEM image at pump–probe zero-time delay with the pump pulse 410 nm (15  $\mu\text{J}/\text{cm}^2$ ) and the probe pulse 273 nm (0.5  $\mu\text{J}/\text{cm}^2$ ). (b) PE intensity traces on different regions.

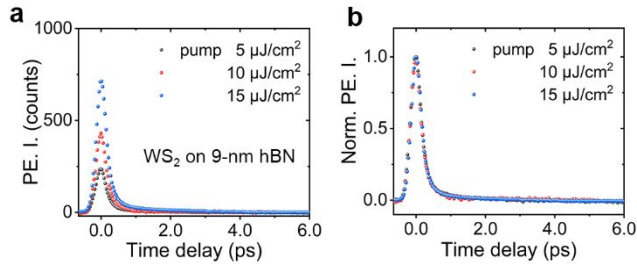


**Figure S10.** PE intensity traces (a) and the normalized ones (b) with different pump fluences for WS<sub>2</sub> on 9-nm hBN.

The evolutions of electron energy distribution in time, for WS<sub>2</sub> on the three regions with the pump wavelength of 410 nm, are shown in Figure S11a–c. The fluences of pump and probe pulses were 10  $\mu\text{J}/\text{cm}^2$  and 0.5  $\mu\text{J}/\text{cm}^2$ , respectively. The EDCs at 0-ps time delay are shown in Figure S11d,e. Despite the large difference in PE intensity for WS<sub>2</sub> on different regions, the EDCs after normalization are similar, and the differences among different regions are comparable to energy resolution of around 150 meV. It should be noted the EDCs discussed

above were obtained by subtracting the background signals before pump–probe zero point. The contribution from secondary electrons should be weakened or eliminated under this operation. Therefore, the EDCs are dominated by pump–probe signals, which represent the populations of photoexcited electrons in conduction band. However, we are not sure if the Auger processes, surface photovoltage effects or in-gap defects have some contributions to the cutoff of EDCs. It should be noted that, the transition from non-equilibrium distribution to hot electron distribution has been demonstrated to be ultrafast (tens of femtoseconds), much shorter than the excitation pulse duration of 120 fs. In addition, we assign the moment with peak PE intensity to the 0-ps time delay, which could be slightly later than the real pump–probe overlapping point, because the number of thermalized electrons in the PE detection window could be larger than that at the instant of photoexcitation due to the electron-electron and electron-photon scattering. Considering the asymmetric EDC at 0-ps time delay, the hot electron distribution should have been formed.

The trap states could be highly localized in real space and delocalized in reciprocal space, and could be within the PE detection window shown in Figure 3 of the main text. However, no signal from the trap states were observed in the EDCs, which implies that the PE efficiency of electrons from trap states are much lower than that from conduction bands.

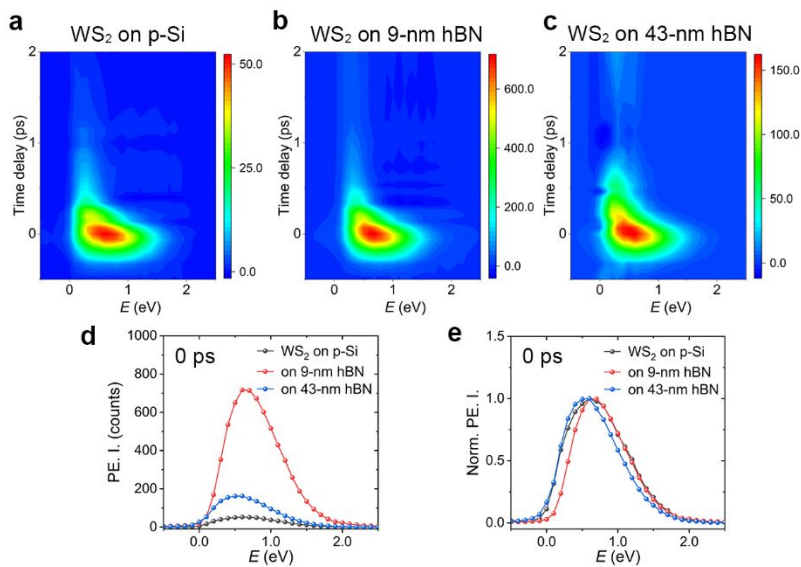


**Figure S11.** (a–c) Mapping of the PE intensity versus the energy and time delay for the WS<sub>2</sub> on

the three regions with the pump wavelength of 410 nm. The EDCs at 0-ps time delay and the normalized EDCs are shown in (d,e).

We also performed TR-PEEM measurements with other pump wavelengths, e.g. 590 nm, by using OPO. More importantly, we noticed the change of decay traces with the accumulated measurement time, as shown in Figure S12. The decay time decreases slowly with PEEM measurement days, indicating the increase of defects at a slow rate, and such a slow rate is possibly due to the low laser fluences.

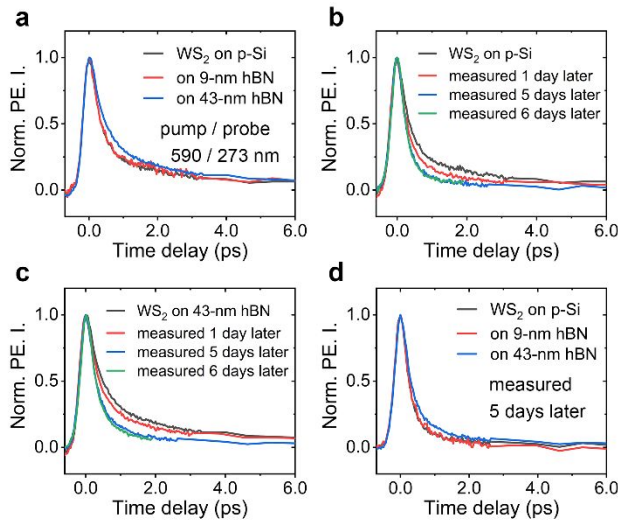


**Figure S12.** (a) Normalized PE intensity traces for WS<sub>2</sub> on the three regions with the pump wavelength of 590 nm. (b,c) Decay traces measured at different days for WS<sub>2</sub> on p-Si and 43-nm hBN, respectively. (d) Decay traces measured 5 days later than that in (a). The decay time decreases slowly with PEEM measurement days, indicating the increase of defects with laser illumination at a slow rate.

We also performed the time- and energy-resolved PEEM measurements with the pump wavelength of 590 nm, as shown Figure S13. The trend of EDCs is similar as that with the pump wavelength of 410 nm, except that the populations in energy are lower owing to the lower photon energy. In addition, the EDCs with pump wavelengths of 590 nm and 410 nm have the same cutoff edge. The EDCs were also fitted with Fermi–Dirac distribution as discussed in the main text. It should be noted that the fitting method is not so strict, since the real density of states was not adopted. The density of states was simplified as the form of square root, considering the

increasing tendency of density of states with energy and the limited PE detection window.

It should be noted that, in our energy-resolved PEEM experiments, we can only obtain the relative values of photoemitted electron energy from the energy analyzer. That is to say, we could obtain the EDCs but not knowing the absolute electron energy. We found that the cutoff edge of different EDCs obtained with different pump wavelengths and from different sample regions are nearly at identical energy. Hence, we set the cutoff edge in the energy axis of EDCs to be energy zero. Considering the band diagram of  $\text{WS}_2$  as shown in Figure 3 of the main text, the energy zero is likely at the conduction band edge of Q valley (lowest energy in the PE detection window).

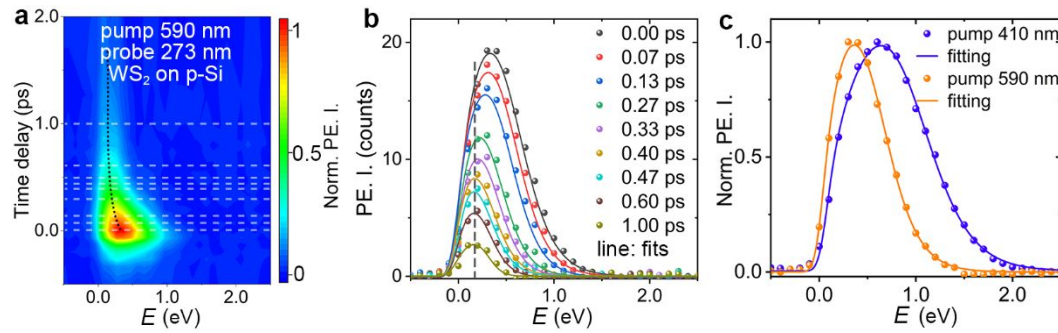


**Figure S13.** (a) Mapping of the PE intensity versus the energy and time delay for the  $\text{WS}_2$  on the p-Si with the pump wavelength of 590 nm. (b) Crosscuts from (a) and fittings of the EDCs with Fermi–Dirac distributions. (c) Comparison of the EDCs at 0-ps time delay with the pump wavelengths of 410 and 590 nm, the electronic temperature with 590 nm (1900 K) is approximately 900 K lower than that with 410 nm (2800 K).

## 6. PEEM measurements for the suspended $\text{WS}_2$

The static PEEM images with different excitation wavelengths and incident angles are shown in Figure S14. The bright spot could be seen with the excitation wavelength of 410 nm at normal incidence, as shown in Figure S14b,e. To eliminate the bright spot, we used oblique incidence with s-polarization, as shown in Figure S14c,f, in which the interference patterns are observed. However, the decay traces with the normal and oblique incidences overlap well, proving that the carrier dynamics are independent of pump fluence, but correlated to defects introduced slowly by

accumulated laser illumination. We performed TR-PEEM measurements at normal incidence with different pump fluences, also showing that the decay time is not sensitive to pump fluence, as shown in Figure S15.

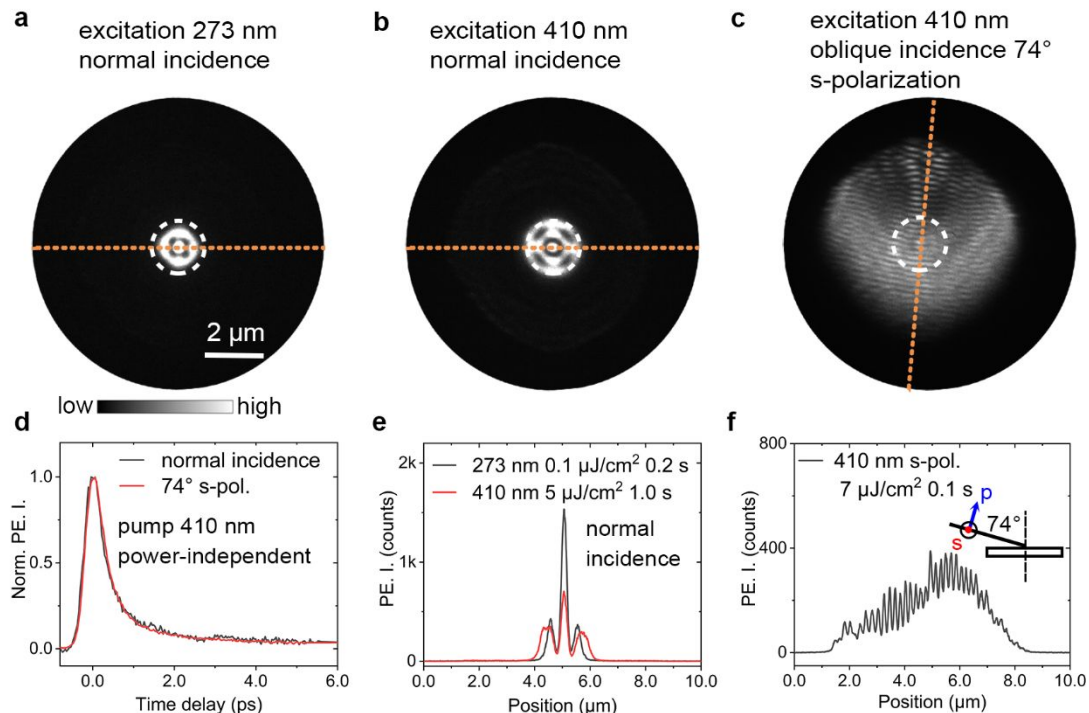


**Figure S14.** (a,b) Static PEEM images with excitation wavelengths of 273 nm ( $0.1 \mu\text{J}/\text{cm}^2$ ) and 410 nm ( $5 \mu\text{J}/\text{cm}^2$ ), respectively, at normal incidence. The crosscuts along the yellow line are shown in (e). (c) Static PEEM image with the excitation wavelength of 410 nm ( $7 \mu\text{J}/\text{cm}^2$ ) at oblique incidence of  $74^\circ$ , with s-polarization. The crosscut along the yellow line is shown in (f). (d) Decay traces extracted from the central region (marked by white dashed circle) with the pump wavelength of 410 nm at normal and oblique incidences, indicating the carrier dynamics are independent of pump fluence.

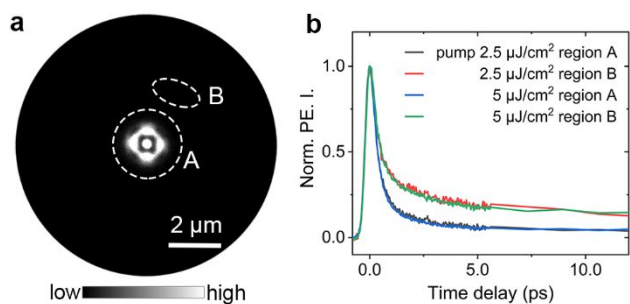


**Figure S15.** (a) TR-PEEM image with the pump pulse 410 nm ( $5 \mu\text{J}/\text{cm}^2$ ) and the probe pulse 273 nm ( $0.1 \mu\text{J}/\text{cm}^2$ ) at 0-ps time delay. (b) Decay traces with pump fluences of  $2.5 \mu\text{J}/\text{cm}^2$  and  $5 \mu\text{J}/\text{cm}^2$

$\mu\text{J}/\text{cm}^2$  on the two regions marked in (a).

We did the probe–fluence dependence experiment, with the similar method for pump fluence, as shown in Figure S16, proving that the carrier dynamics are also independent of probe fluence in a short time.

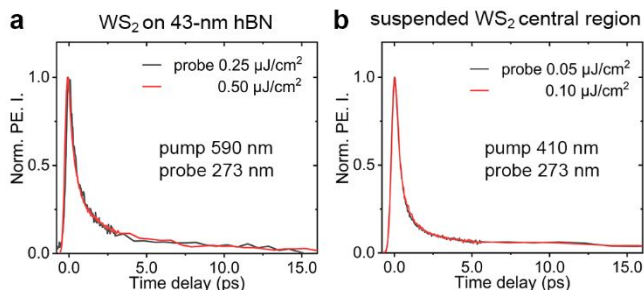


**Figure S16.** Normalized PE intensity traces with different probe fluences for WS<sub>2</sub> on 43-nm hBN (a) and suspended WS<sub>2</sub> in the central region (b). The pump pulses were set as 590 nm (19  $\mu\text{J}/\text{cm}^2$ ) in (a) and 410 nm (5  $\mu\text{J}/\text{cm}^2$ ) in (b).

## 7. Movie of TR-PEEM signals for the supported WS<sub>2</sub>

The movie shows pump–probe PEEM signals at a series of time delays with the pump pulse 410 nm (10  $\mu\text{J}/\text{cm}^2$ ) and the probe pulse 273 nm (0.5  $\mu\text{J}/\text{cm}^2$ ) at normal incidence.

## REFERENCES

- (1). Lien, D.-H.; Kang, J. S.; Amani, M.; Chen, K.; Tosun, M.; Wang, H.-P.; Roy, T.; Eggleston, M. S.; Wu, M. C.; Dubey, M.; Lee, S.-C.; He, J.-H.; Javey, A., Engineering Light Outcoupling in 2D Materials. *Nano Lett.* **2015**, *15*, 1356–1361.
- (2). Yoon, D.; Moon, H.; Son, Y.-W.; Choi, J. S.; Park, B. H.; Cha, Y. H.; Kim, Y. D.; Cheong, H., Interference effect on Raman spectrum of graphene on SiO<sub>2</sub>/Si. *Phys. Rev. B* **2009**, *80*, 125422.
- (3). Raja, A.; Chaves, A.; Yu, J.; Arefe, G.; Hill, H. M.; Rigosi, A. F.; Berkelbach, T. C.; Nagler, P.; Schüller, C.; Korn, T.; Nuckolls, C.; Hone, J.; Brus, L. E.; Heinz, T. F.; Reichman, D. R.; Chernikov, A., Coulomb engineering of the bandgap and excitons in two-dimensional materials. *Nat. Commun.* **2017**, *8*, 15251.

- (4). Lee, S.-Y.; Jeong, T.-Y.; Jung, S.; Yee, K.-J., Refractive Index Dispersion of Hexagonal Boron Nitride in the Visible and Near-Infrared. *Phys. Status Solidi (b)* **2019**, *256*, 1800417.
- (5). Nan, H.; Wang, Z.; Wang, W.; Liang, Z.; Lu, Y.; Chen, Q.; He, D.; Tan, P.; Miao, F.; Wang, X.; Wang, J.; Ni, Z., Strong Photoluminescence Enhancement of MoS<sub>2</sub> through Defect Engineering and Oxygen Bonding. *ACS Nano* **2014**, *8*, 5738–5745.
- (6). Venkatakrisnan, A.; Chua, H.; Tan, P.; Hu, Z.; Liu, H.; Liu, Y.; Carvalho, A.; Lu, J.; Sow, C. H., Microsteganography on WS<sub>2</sub> Monolayers Tailored by Direct Laser Painting. *ACS Nano* **2017**, *11*, 713–720.
- (7). Ardekani, H.; Younts, R.; Yu, Y.; Cao, L.; Gundogdu, K., Reversible Photoluminescence Tuning by Defect Passivation via Laser Irradiation on Aged Monolayer MoS<sub>2</sub>. *ACS Appl. Mater. Interfaces* **2019**, *11*, 38240–38246.
- (8). Jung, G.-H.; Yoo, S.; Park, Q.-H., Measuring the optical permittivity of two-dimensional materials without a priori knowledge of electronic transitions. *Nanophotonics* **2018**, *8*, 263–270.